Hindawi
Journal of Advanced Transportation
Volume 2022, Article ID 5769224, 16 pages
https://doi.org/10.1155/2022/5769224

Research Article

Design of Coupling Coil Parameters for Wireless Charging Tram Based on Electromagnetic Safety

Sanmu Xiu,[1] **Wenmei Hao**,[2] **Ying Zhou**,[3] **and Fengyu Leng**[4]

[1]*School of Electrical Engineering, Beijing Jiaotong University, Beijing 100044, China*
[2]*School of Mechanical Engineering, Beijing Institute of Technology, Beijing 100081, China*
[3]*CRRC, Qingdao Sifang, Shandong 266100, China*
[4]*Institute of Electrical Engineering, Chinese Academy of Sciences, Beijing 100190, China*

Correspondence should be addressed to Sanmu Xiu; smxiu@bjtu.edu.cn

Received 17 February 2022; Revised 8 April 2022; Accepted 15 April 2022; Published 9 May 2022

Academic Editor: Ren-Yong Guo

As a new type of urban rail transit tram, wireless charging tram uses high frequency electromagnetic field to conduct inductive power transmission, which gets rid of the traditional overhead catenary network, but inevitably causes electromagnetic radiation to the surrounding environment. Research shows that excessive electromagnetic radiation will affect the normal operation of equipment and the safety of human body. This paper analyzes the structure and coil configuration of the dynamic charging system for wireless charging tram. Aiming at the problem of electromagnetic radiation, a mathematical model with minimum electromagnetic radiation as the target and system parameters as the constraint condition is established. Finally, the system parameters of the electromagnetic coupling mechanism of the wireless charging tram are designed and optimized. The simulation and experimental results show that the method can meet the operating requirements of the system and reduce the electromagnetic radiation to the surrounding environment.

1. Introduction

As a new type of urban rail transit tram, the wireless charging trams adopt the inductive power transmission (IPT) technology for power transmission, so that the power supply system and the tram can transmit power without physical contact. The IPT technology not only solves the disadvantages brought by the traditional contact power supply mode, such as easy loss, contact spark, carbon accumulation, difficult maintenance, high construction cost, but also improves the safety, reliability, and flexibility of tram operation [1–3]. The application of IPT technology to urban rail transit trams needs to meet the high power and high efficiency power supply requirements of the rail transit system as well as the electromagnetic safety requirements that will not affect the normal operation of equipment in the surrounding environment and the safety of human body. As the main body of energy transmission in the inductively coupled power transmission system, the laying mode and parameter design of the coupling coil will have a direct impact on the energy transmission power, efficiency, and external electromagnetic radiation, so the research on the coupling coil is particularly important [4–6].

At present, many scholars have carried out a series of studies on the coupling coil in IPT system, which can be roughly divided into coil structure optimization design and electromagnetic radiation research. First, in terms of coil design, [7] proposed a DLDD type coil structure for electric trams from the perspective of coil shape design, analyzed and proved that it has a good deviation tolerance. In [8], the magnetic circuit model of the coupling system when the primary and secondary coils are open is established. By deducing the approximate calculation formulas of the inductance and coupling coefficient of the primary and secondary coils, the magnetic core structure is optimized and the transmission capacity of the system is enhanced. References [9, 10] improves the efficiency or output power of the system by increasing the number of parallel primary and

secondary coils. Combined with the existing literature of coil optimization design, the optimization goal is mainly focused on improving the output performance of the system, such as power and efficiency. By using different optimization processes and evaluation methods for a certain power or efficiency index, the performance parameters of a certain aspect of the coupling coil are optimized. Then, in terms of electromagnetic radiation research, [11] analyzed and concluded that the electromagnetic environment of wireless charging meets the relevant standards of the INCIRP guidelines [12]. Reference [13] evaluated the electromagnetic safety of the radio energy transmission system, and concluded that when the distance between the human body and the radio energy transmission system is 12 cm, the electromagnetic environment in which the human body lies flat behind the tram meets the electromagnetic safety requirements. Reference [14] analyzed the electromagnetic radiation of the radio energy transmission system and found that when the human body is close to the chassis, the nearest safe distance between the body and the coil center is 0.8 meters. The current research focuses on the electromagnetic radiation analysis of the coupling coil mechanism, and the safe distance of electromagnetic radiation is obtained according to the existing electromagnetic radiation standards. To sum up, at present, the research on coil design and electromagnetic radiation is basically split, and there is lack of considering the actual tram structure and parameters.

Based on the application background of induction-coupled power transmission technology for wireless charging tram, this paper analyzes the coil configuration method applicable to dynamic charging of wireless charging tram, and gives the specific design method of coil mutual inductance, number of turns, and other parameters. Considering that the induction power transmission technology utilizes the coupling of high frequency electromagnetic field to realize the power transmission, part of the high frequency electromagnetic energy will inevitably enter the surrounding environment and bring electromagnetic safety problems to the surrounding environment. Therefore, aiming at the safety of electromagnetic radiation in inductively coupled power transmission technology, a mathematical model with system parameter constraint is proposed with minimum electromagnetic radiation as the target. Finally, the system parameters of electromagnetic coupling mechanism of wireless charging tram are designed globally. Simulation and experimental results show the effectiveness of the design optimization method.

2. Structure Analysis of IPT system

2.1. Coil Structure Analysis of IPT System. Coil shapes commonly used in IPT systems include round, rectangular, and combined (DD) coils [15]. Electromagnetic analysis was conducted on the coils of three shapes, and the geometry and distribution of magnetic field intensity obtained is shown in Figure 1.

As can be seen from Figure 1, the magnetic field strength of the combined (DD) coil at the center of the coil is obviously greater than that of the circle and rectangle, which is not conducive to reducing electromagnetic radiation. Moreover, the combined (DD) coil is complex and expensive to wind. Therefore, the combined (DD) coil is not suitable for the wireless charging tram. The mutual inductance and coupling coefficient of circular and rectangular coils are analyzed with the change of air gap, and the results are shown in Figure 2.

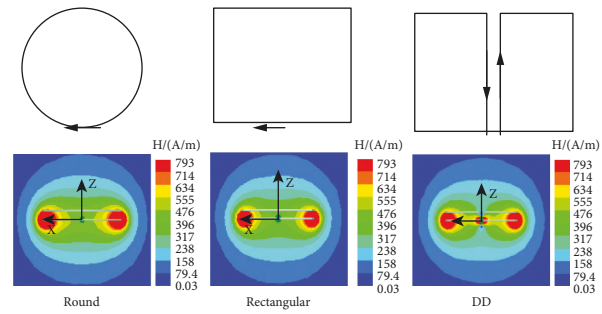

Figure 1: Magnetic field intensity distribution of different coil structures in the XZ plane.

The circular coil has a consistent direction and is highly sensitive to coil migration, so it is not suitable for rail transit trams based on wireless charging. Not only is the mutual inductance of the rectangular coil greater than that of the circular coil under the same air gap, but also the mutual inductance is more tolerant to the fluctuation of the air gap. At the same time, the rectangular coil is easy to ensure the uniformity of the air gap magnetic field, which is suitable for one-way driving trams. Therefore, the rectangular coil is chosen as the coupling coil shape.

The primary side coil is laid in series in the middle of the track, and the secondary side coil is installed on the bottom of the tram. Therefore, the installation space of the coupling coil of the wireless charging tram puts forward some requirements for the structural design of the coupling coil. Studies have shown that increasing the coil area is conducive to improving the coupling coefficient of primary and secondary coils and enhancing the power transmission capacity [7]. Therefore, in order to make full use of the installation space of the wireless charging tram, the size of the side coil is aimed at maximizing the assembly space provided by the tram. This paper proposes the coil configuration as shown in Figure 3. The two secondary coils are, respectively, installed in the two installation spaces under the motor trains, and the size of the coils is basically consistent with the installation space. In order to smooth the induced voltage when the secondary coil passes through the primary coil segment, the length of the primary coil is consistent with the spacing between the two secondary coils. In this way, one secondary coil leaves while another secondary coil enters, maintaining the corresponding relationship of the primary and secondary coils.

2.2. Topology Analysis of IPT System. In the IPT system, the gap between the primary coil and the secondary coil makes the coupling coil have a large leakage inductance. If not compensated, it will greatly affect the power transmission

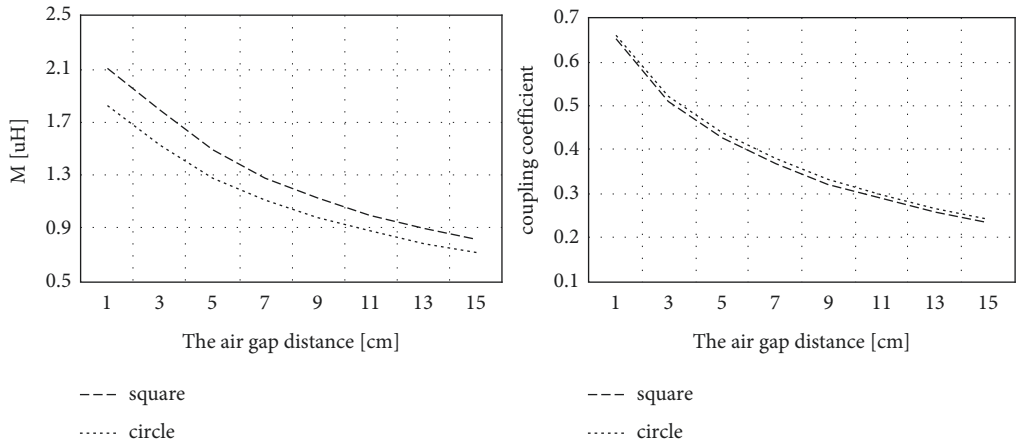

Figure 2: Mutual inductance M and coupling coefficient vary with air gap fluctuation.

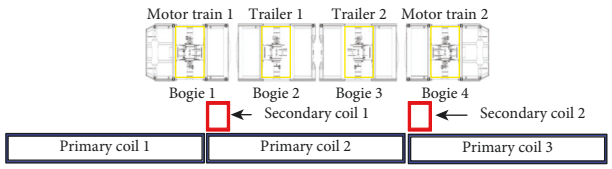

Figure 3: Configuration of couping coils.

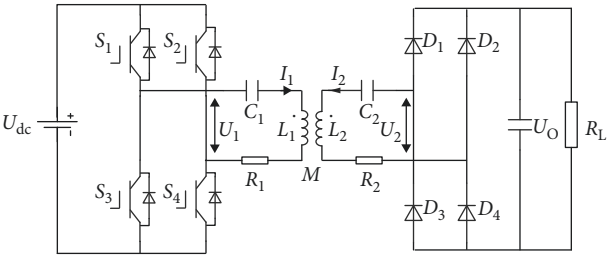

Figure 4: Circuit topology of wireless power transmission system.

capacity of the system and at the same time increase the voltage and current stress borne by the power devices. To solve this problem, the capacitance and inductance can be connected in series or in parallel between the primary coil and the secondary coil. The compensation method can be divided into unit compensation, two component compensation, and three component compensation. The unit compensation includes series-series (SS) compensation, series-parallel (SP) compensation, parallel-series (PS) compensation, and parallel-parallel (PP) compensation. The compensation of two components is LCL-S and the compensation of three components is LCC-S. The series-series (SS) compensation has the characteristics of simple structure and constant output voltage. In addition, the value of series-series compensation capacitance is independent of the mutual inductance between the coupling coils and the load size, which is suitable for the condition of mutual inductance and load fluctuation in the movement of the tram without network. Therefore, this paper adopts the series-series compensation (SS) topology, whose circuit topology is shown in Figure 4 [16].

In Figure 4, the excitation source of the transmitting side is the DC voltage source U_{dc}. S_1, S_2, S_3, and S_4 are insulated-gate bipolar transistors that make up the high frequency inverter circuit. R_1 and R_2 are the resistors of the primary coil and the secondary coil, respectively. L_1 and L_2 are the self-equivalent inductance of primary coil and secondary coil, respectively. M is the mutual inductance between the primary coil and the secondary coil, and C_1 and C_2 are the compensation capacitance of the transmitting end and the receiving end, respectively. D_1, D_2, D_3, and D_4 are diodes that make up the rectifier. R_L is the load resistance. When the system is in operation, the primary and secondary coils are matched to the same resonant frequency by compensating capacitors C_1 and C_2. The inverter circuit generates high frequency alternating current, which provides energy for the primary coil. The frequency of AC is the same as the resonant frequency of the primary circuit. Electromagnetic induction then enables the energy to be efficiently transmitted to the secondary coil. The current generated by the secondary coil is fed to the load through the rectifying and filtering device, so as to realize the wireless transmission of the whole system.

The simplified model of the IPT circuit is shown in Figure 5 [17].

In Figure 5, R is the equivalent resistance before the rectifier bridge, and M is the mutual inductance between the primary coil and the secondary coil. U_1 is the AC voltage source obtained from the DC voltage source through the full-bridge inverter, and then the system meets the following requirements [18]:

$$\begin{cases} U_1 = \dfrac{2\sqrt{2}\,U_{dc}}{\pi} \\ U_2 = \dfrac{2\sqrt{2}\,U_O}{\pi} \\ R = \dfrac{8}{\pi^2} R_L \end{cases} . \tag{1}$$

Under sinusoidal steady state operation of the ac voltage source, the circuit impedance Z_1 of the primary coil and the

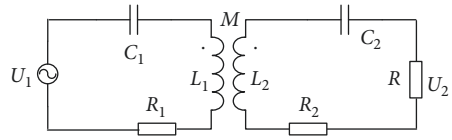

Figure 5: Circuit model of wireless power transmission system.

circuit impedance Z_2 of the secondary coil are expressed as follows:

$$\begin{cases} \mathbf{Z}_1 = j\omega L_1 + \dfrac{1}{j\omega C_1} + R_1 \\ \\ \mathbf{Z}_2 = j\omega L_2 + \dfrac{1}{j\omega C_2} + R_2 \end{cases}, \tag{2}$$

where the primary and secondary coils are resonant at frequency ω, namely,

$$\begin{cases} j\omega L_1 + \dfrac{1}{j\omega C_1} = 0 \\ \\ j\omega L_2 + \dfrac{1}{j\omega C_2} = 0 \end{cases}. \tag{3}$$

At this point, the output power and efficiency of the system are

$$P_{\text{out}} = \frac{U_1^2 \omega^2 M^2 R}{\left[\omega^2 M^2 + R_1 (R_2 + R)\right]^2}, \tag{4}$$

$$\eta = \frac{\omega^2 M^2 R}{\left[\omega^2 M^2 + R_1 (R_2 + R)\right](R_2 + R)}. \tag{5}$$

According to formulas (4) and (5), the output power and efficiency of the system are directly affected by the mutual inductance between the coupling coils and the size of the internal resistance, which in turn are related to the number and size of the coils. Therefore, it is necessary to design the coil parameters reasonably so as to meet the requirements of output power and efficiency of the system.

3. Design of Coupling Parameters of IPT System

3.1. Coil Structure Analysis of IPT System. Mutual inductance is one of the important parameters in the design of coupling coil. According to Neumann formula, the calculation formulas of self-induction of the rectangular coil and mutual inductance between coils are, respectively, [19]

$$L = \frac{\mu_0}{4\pi}\left[a \ln \frac{2ab}{r\left(a + \sqrt{a^2 + b^2}\right)} + b \ln \frac{2ab}{r\left(a + \sqrt{a^2 + b^2}\right)} - 2\left(a + b - \sqrt{a^2 + b^2}\right) + \frac{a + b}{4}\right]. \tag{6}$$

$$M = \frac{\mu_0}{4\pi} \oint_{l_1} \oint_{l_2} \frac{dl_1 dl_2}{R}, \tag{7}$$

where a, b, and r are the length and width of the rectangular coil and the cross-section radius of the wire, respectively. μ_0 is the permeability in vacuum. Therefore, when the structure parameters of the coil are determined, the self-inductance of the primary coil and the secondary coil and the mutual inductance of the coupling coil can be calculated as L_{10}, L_{20}, and M_0, respectively, in the case of single turn. If the number of turns and the self-induction of primary coil and secondary coil are N_1, N_2, L_1, and L_2, respectively, then

$$M \approx N_1 N_2 M_0, \tag{8}$$

$$L_1 \approx {N_1}^2 L_{10}. \tag{9}$$

$$L_2 \approx {N_2}^2 L_{20}. \tag{10}$$

According to formulas (6)–(10), the self-inductance and mutual inductance parameters of the coupling coil can be calculated by determining the structure of the coupling coil.

3.2. Calculation of Coil Magnetic Field Parameters. According to the analysis, when the coupling coil is working, the working area satisfies the condition of quasistatic magnetic field [20]. According to classical Maxwell's equations, the following relation can be obtained:

$$\mathbf{A} = \frac{\mu}{4\pi} \cdot \int_V \frac{\mathbf{J}}{R} dV. \tag{11}$$

The curl of both ends of (12) can be obtained, and the expression of magnetic induction intensity can be obtained.

$$\mathbf{B} = \frac{\mu}{4\pi} \int_v \mathbf{J} \times \frac{\mathbf{R}}{R^3} dV, \tag{12}$$

where R is the distance vector between the field source and the measurement point. For isotropic media, the following relationships exist:

$$\mathbf{B} = \mu \mathbf{H}. \tag{13}$$

Therefore, the formula for calculating the magnetic field strength is

$$\mathbf{H} = \frac{1}{4\pi} \int_v \mathbf{J} \times \frac{\mathbf{R}}{R^3} dV. \tag{14}$$

For the rectangular coil, it can be regarded as four segments of finite length direct current-carrying wire. Each wire is calculated, and then the spatial electromagnetic field strength of the rectangular planar coupling coil is obtained by means of vector superposition. For multi-turn coils, they can be equivalent to multiple concentric rectangles as shown in Figure 6 for calculation.

$$\begin{aligned} L_{1n} &= 2a_1 + 2\ d(N_1 - 1), \\ W_{2n} &= 2b_2 + 2\ d(N_2 - 1), \\ L_{2n} &= 2a_2 + 2\ d(N_2 - 1), \\ W_{1n} &= 2b_1 + 2\ d(N_1 - 1). \end{aligned} \tag{15}$$

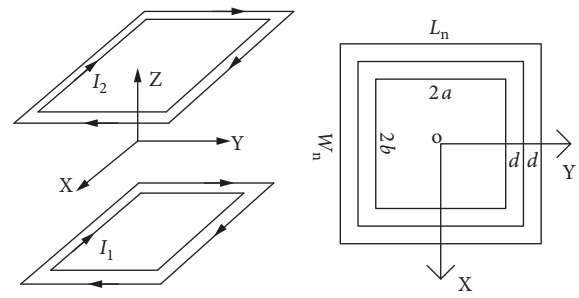

Figure 6: Coordinate diagram of coaxial multi-turn transmitting coil and receiving coil.

In Figure 6, the center point of the center plane parallel to the primary coil and the secondary coil is the origin of coordinates. The axis perpendicular to the central plane is the Z-axis. The axis passing through the origin perpendicular to the Z-axis and parallel to the forward axis is the X-axis. The axis perpendicular to the origin and parallel to the right is the Y-axis. Set the current of the two-current coil in the same direction. The current in the transmitting coil is I_1, and the current in the receiving coil is I_2. The primary coil is 2c away from the secondary coil. The number of turns of the primary side coil is N_1, and the number of turns of the secondary side coil is N_2. The length of the primary coil of the first turn is $2a_1$, and the width of the coil is $2b_1$. The length of the secondary coil of the first turn is $2a_2$, and the width of the coil is $2b_2$. The length of the Nth layer of the original side coil is L_{1n} and the width is W_{1n}. The length of the Nth layer of the secondary side coil is L_{2n}, and the width is W_{2n}. The spacing between the adjacent turns is d, so:

Then, the magnetic field strength of the rectangular coupling coil at any point in the space is, respectively, the components of the X-axis, Y-axis, and Z-axis.

$$\begin{aligned} H_x = \frac{I_1}{4\pi}\sum_{n=1}^{N_1}&\left[\frac{z+c}{\left[(L_{2n}/2-x)^2+(z+c)^2\right]}\left(\frac{W_{2n}/2+y}{\sqrt{(L_{2n}/2-x)^2+(w_{2n}/2+y)^2+(z+c)^2}}+\frac{w_{2n}/2-y}{\sqrt{(L_{2n}/2-x)^2+(w_{2n}/2-y)^2+(z+c)^2}}\right)-\frac{z+c}{\left[(L_{2n}/2+x)^2+(z+c)^2\right]}\right. \\ &\left.\times\left(\frac{w_{2n}/2-y}{\sqrt{(L_{2n}/2+x)^2+(w_{2n}/2-y)^2+(z+c)^2}}+\frac{w_{2n}/2+y}{\sqrt{(L_{2n}/2+x)^2+(w_{2n}/2+y)^2+(z+c)^2}}\right)\right] \\ +\frac{I_2}{4\pi}\sum_{n=1}^{N_2}&\left[\frac{z-c}{\left[(L_{1n}/2-x)^2+(z-c)^2\right]}\left(\frac{w_{1n}/2+y}{\sqrt{(L_{1n}/2-x)^2+(L_{1n}/2+y)^2+(z-c)^2}}+\frac{w_{1n}/2-y}{\sqrt{(L_{1n}/2-x)^2+(w_{1n}/2-y)^2+(z-c)^2}}\right)-\frac{z-c}{\left[(L_{1n}/2+x)^2+(z-c)^2\right]}\right. \\ &\left.\times\left(\frac{w_{1n}/2-y}{\sqrt{(L_{1n}/2+x)^2+(w_{1n}/2-y)^2+(z-c)^2}}+\frac{w_{1n}/2+y}{\sqrt{(L_{1n}/2+x)^2+(w_{1n}/2+y)^2+(z-c)^2}}\right)\right] \end{aligned} \tag{16}$$

$$H_y = \frac{I_1}{4\pi}\sum_{n=1}^{N_1}\left[\frac{z+c}{\left[(W_{2n}/2-y)^2+(z+c)^2\right]}\left(\begin{array}{c}\dfrac{L_{2n}/2+x}{\sqrt{(L_{2n}/2+x)^2+(W_{2n}/2+y)^2+(z+c)^2}} \\ +\dfrac{L_{2n}/2-x}{\sqrt{(L_{2n}/2-x)^2+(W_{2n}/2+y)^2+(z+c)^2}}\end{array}\right)-\frac{z+c}{\left[(W_{2n}/2+y)^2+(z+c)^2\right]}\right.$$
$$\left.\times\left(\frac{L_{2n}/2+x}{\sqrt{(L_{2n}/2+x)^2+(W_{2n}/2+y)^2+(z+c)^2}}+\frac{L_{2n}/2-x}{\sqrt{(L_{2n}/2-x)^2+(W_{2n}/2+y)^2+(z+c)^2}}\right)\right]$$

$$+\frac{I_2}{4\pi}\sum_{n=1}^{N_2}\left[\begin{array}{l}\dfrac{z-c}{\left[\left(W_{1n}/2-y\right)^2+\left(z-c\right)^2\right]}\left(\begin{array}{l}\dfrac{L_{1n}/2+x}{\sqrt{\left(L_{1n}/2+x\right)^2+\left(W_{1n}/2+y\right)^2+\left(z-c\right)^2}}\\ +\dfrac{L_{1n}/2-x}{\sqrt{\left(L_{1n}/2-x\right)^2+\left(W_{1n}/2+y\right)^2+\left(z-c\right)^2}}\end{array}\right)-\dfrac{z-c}{\left[\left(W_{1n}/2+y\right)^2+\left(z-c\right)^2\right]}\\ \times\left(\dfrac{L_{1n}/2+x}{\sqrt{\left(L_{1n}/2+x\right)^2+\left(W_{1n}/2+y\right)^2+\left(z-c\right)^2}}+\dfrac{L_{1n}/2-x}{\sqrt{\left(L_{1n}/2-x\right)^2+\left(W_{1n}/2+y\right)^2+\left(z-c\right)^2}}\right)\end{array}\right]. \tag{17}$$

$$H_z=\frac{I_1}{4\pi}\sum_{n=1}^{N_1}\left[\begin{array}{l}\dfrac{\left(W_{2n}/2+y\right)}{\left[\left(W_{2n}/2+y\right)^2+\left(z+c\right)^2\right]}\left(\dfrac{L_{2n}/2+x}{\sqrt{\left(L_{2n}/2+x\right)^2+\left(W_{2n}/2+y\right)^2+\left(z+c\right)^2}}+\dfrac{L_{2n}/2-x}{\sqrt{\left(L_{2n}/2-x\right)^2+\left(W_{2n}/2+y\right)^2+\left(z+c\right)^2}}\right)+\dfrac{\left(W_{2n}/2-y\right)}{\left[\left(W_{2n}/2-y\right)^2+\left(z+c\right)^2\right]}\\ \times\left(\dfrac{L_{2n}/2+x}{\sqrt{\left(L_{2n}/2+x\right)^2+\left(W_{2n}/2-y\right)^2+\left(z+c\right)^2}}+\dfrac{L_{2n}/2-x}{\sqrt{\left(L_{2n}/2-x\right)^2+\left(W_{2n}/2-y\right)^2+\left(z+c\right)^2}}\right)\\ +\dfrac{\left(L_{2n}/2-x\right)}{\left[\left(L_{2n}/2-x\right)^2+\left(z+c\right)^2\right]}\left(\dfrac{W_{2n}/2+y}{\sqrt{\left(L_{2n}/2-x\right)^2+\left(W_{2n}/2+y\right)^2+\left(z+c\right)^2}}+\dfrac{W_{2n}/2-y}{\sqrt{\left(L_{2n}/2-x\right)^2+\left(W_{2n}/2-y\right)^2+\left(z+c\right)^2}}\right)+\dfrac{\left(L_{2n}/2+x\right)}{\left[\left(L_{2n}/2+x\right)^2+\left(z+c\right)^2\right]}\\ \times\left(\dfrac{W_{2n}/2-y}{\sqrt{\left(L_{2n}/2+x\right)^2+\left(W_{2n}/2-y\right)^2+\left(z+c\right)^2}}+\dfrac{W_{2n}/2+y}{\sqrt{\left(L_{2n}/2+x\right)^2+\left(W_{2n}/2+y\right)^2+\left(z+c\right)^2}}\right)\end{array}\right]$$

$$+\frac{I_2}{4\pi}\sum_{n=1}^{N_2}\left[\begin{array}{l}\dfrac{\left(W_{1n}/2+y\right)}{\left[\left(W_{1n}/2+y\right)^2+\left(z-c\right)^2\right]}\left(\dfrac{L_{1n}/2+x}{\sqrt{\left(L_{1n}/2+x\right)^2+\left(W_{1n}/2+y\right)^2+\left(z-c\right)^2}}+\dfrac{L_{1n}/2-x}{\sqrt{\left(L_{1n}/2-x\right)^2+\left(W_{1n}/2+y\right)^2+\left(z-c\right)^2}}\right)+\dfrac{\left(W_{1n}/2-ty\right)}{\left[\left(W_{1n}/2-y\right)^2+\left(z-c\right)^2\right]}\\ \times\left(\dfrac{L_{1n}/2+x}{\sqrt{\left(L_{1n}/2+x\right)^2+\left(W_{1n}/2-y\right)^2+\left(z-c\right)^2}}+\dfrac{L_{1n}/2-x}{\sqrt{\left(L_{1n}/2-x\right)^2+\left(W_{1n}/2-y\right)^2+\left(z-c\right)^2}}\right)\\ +\dfrac{\left(L_{1n}/2-x\right)}{\left[\left(L_{1n}/2-x\right)^2+\left(z-c\right)^2\right]}\left(\dfrac{W_{1n}/2+y}{\sqrt{\left(L_{1n}/2-x\right)^2+\left(W_{1n}/2+y\right)^2+\left(z-c\right)^2}}+\dfrac{W_{1n}/2-y}{\sqrt{\left(L_{1n}/2-x\right)^2+\left(W_{1n}/2-y\right)^2+\left(z-c\right)^2}}\right)+\dfrac{\left(L_{1n}/2+x\right)}{\left[\left(L_{1n}/2+x\right)^2+\left(z-c\right)^2\right]}\\ \times\left(\dfrac{W_{1n}/2-y}{\sqrt{\left(L_{1n}/2+x\right)^2+\left(W_{1n}/2-y\right)^2+\left(z-c\right)^2}}+\dfrac{W_{1n}/2+y}{\sqrt{\left(L_{1n}/2+x\right)^2+\left(W_{1n}/2+y\right)^2+\left(z-c\right)^2}}\right)\end{array}\right]. \tag{18}$$

The derivation process is given in appendix. The magnetic field strength of the rectangular coupling coil at any point in space is

$$H=\sqrt{H_x^2+H_y^2+H_z^2}. \tag{19}$$

According to formulae (16) to (19), the magnetic field strength is related to the current in the coil, the coil size, the coil turn spacing, and the coil turn number. Among them, the current in the coil is determined by the system power, voltage, and the compensation topology of the main circuit, and the coil size and coil turn spacing are determined by the actual installation space and configuration mode. Therefore, the number of turns of the coupling coil can be optimized according to the magnetic field strength.

3.3. Design of Coil Turns Based on Minimum Electromagnetic Radiation

3.3.1. Optimization Target of Turns. When the coupling coil is laid along the *Y*-axis, the electromagnetic analysis is carried out on the coupling coil, and the distribution diagram of the magnetic field intensity in the XZ plane as shown in Figure 7 is obtained. As can be seen from Figure 7, the magnetic field intensity is mainly distributed in the direction of *X*-axis and *Z*-axis. According to the specification for electromagnetic radiation issued by the international commission on non-ionizing radiation protection (ICNIRP) [17], for electromagnetic waves in the 3–150 kHz frequency band that are commonly used in wireless charging, the electromagnetic parameters of the electromagnetic radiation standard are defined as electric field intensity no more than

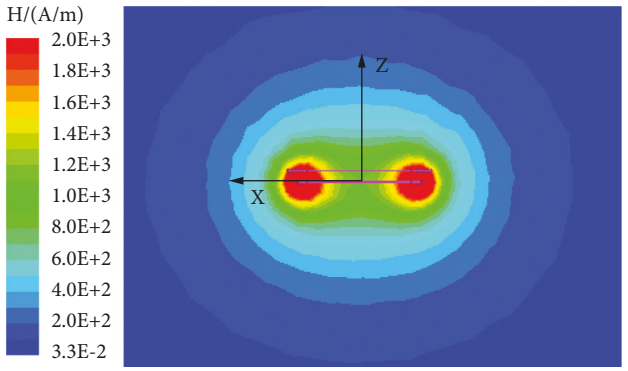

Figure 7: XZ plane magnetic field intensity distribution.

83 V/m, magnetic field intensity no more than 21 A/m, and magnetic flux density no more than 0.027 mT. α is defined as the X-axis distance at the magnetic field strength greater than or equal to 21 A/m. β is defined as the Z-axis distance at the magnetic field strength greater than or equal to 21 A/m. The magnetic field electromagnetic radiation of the system is $\lambda = \max\{\alpha, \beta\}$. When the working voltage U_{dc} of the system is 750 V, the working frequency f is 30 kHz, and the current effective value in the coil is 445 A, the relation curve between the excess range of magnetic field strength and the number of coil turns is obtained as shown in Figure 8.

According to the data, the larger the number of turns of primary coil N_1 and secondary coil N_2, the larger the excess range of electromagnetic radiation and the stronger the magnetic field radiation. Based on the above analysis, this paper takes minimum electromagnetic radiation as the optimization target of coil turns.

3.3.2. Constraint Conditions of Coil Turns Design. In order to ensure the normal operation of the tram, the system must meet the requirements of output power and efficiency at the rated state. According to formulas (4) and (5), the internal resistance of the primary and secondary side coils should also be considered when calculating the output power and efficiency. According to the empirical equations, the equivalent AC impedance ESR of high-frequency Liz wire used by inductive coupling coil can be expressed as

$$ESR = K_c \frac{4\rho l}{\pi N_a D_a^2} \times \left[1 + 2\left(\frac{N_a D_a}{1.155\sqrt{N_a} \times D_a + 0.0508}\right)^2 \left(\frac{D_a\sqrt{f}}{0.262}\right)^4\right], \tag{20}$$

where K_c is the length correction coefficient. ρ is the copper wire resistivity. l is the wire length of the coil. N_a is the number of strands of the single-turn coil. D_a is the diameter of the single-turn coil of the Liz wire, and f is the frequency. Thus, the internal resistances R_1 and R_2 of primary coil and secondary coil can be calculated. If the rated power of the system is expressed by P_N. It is also the power that the wireless energy transmission system needs to provide to ensure the stable operation of the vehicle, and the efficiency and output power P_{out} eta should satisfy

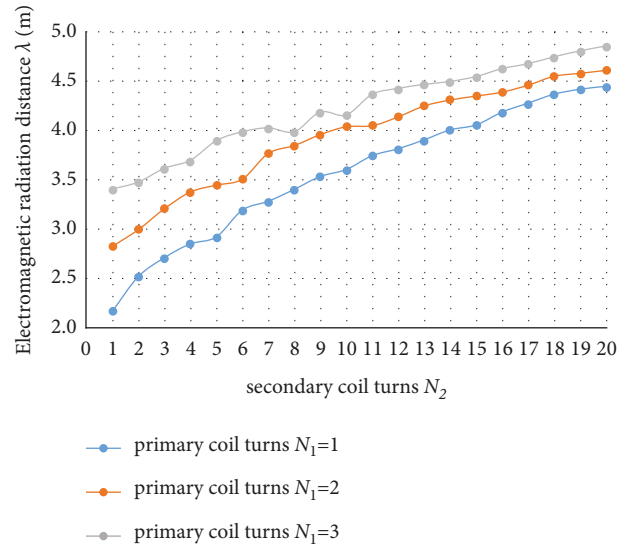

Figure 8: Relationship between magnetic field intensity exceeding limit and coil turns.

$$\begin{aligned} P_{out} &> P_N, \\ \eta &> \eta_{min}. \end{aligned} \tag{21}$$

Based on the above analysis, the mathematical model with minimum electromagnetic radiation as the design objective and system parameters as the constraint condition can be described by the following equation:

$$\begin{cases} \min(\lambda) \\ s.t. \begin{cases} P_{out} \geq P_N \\ \eta \geq \eta_{min} \end{cases} \end{cases} \tag{22}$$

3.3.3. Design Method of Coupling Coil Turns. Coil parameters are designed according to the mathematical model shown in (22). The specific process is: The size and mutual inductance of primary coil and secondary coil are determined according to the structure parameters of the tram body and the input and output requirements of the system. Thus, the initial array of coil parameters is determined, and the number of turns of the primary coil and the number of turns of the secondary coil are determined. Verify whether it meets the constraint condition. Discard the array that does not satisfy the constraint condition, and compare the array that satisfies the constraint condition with the previous set. The group that retained the smaller value of the electromagnetic radiation was compared with the next group. Finally, an optimal set of coil parameters is obtained. The design flow chart is shown in Figure 9.

4. Simulation and Experiment

4.1. Simulation. According to the design of coil parameters, the primary coil is a 20 m * 1 m rectangular coil, and the secondary coil is a 1 m * 1 m square coil. The coil parameters were designed according to the method shown in Figure 9,

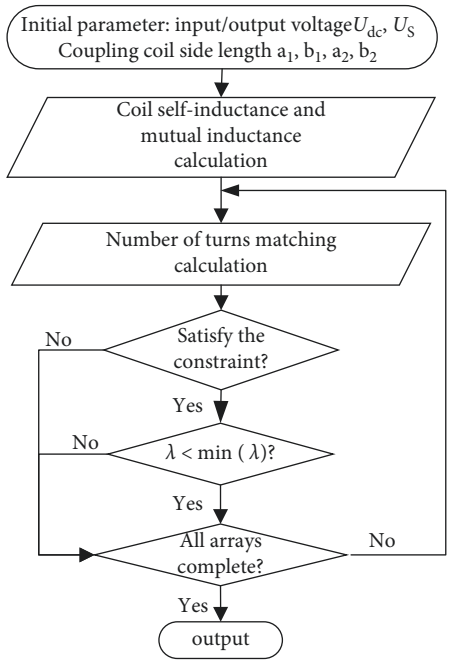

Figure 9: Flow chart of coil parameter design.

and the coil turns obtained were 2 turns for the primary coil and 5 turns for the secondary coil. According to the structure of the tram, the air gap between the primary coil and the secondary coil fluctuates between 37.6 mm and 127 mm. According to literature [19], the mutual inductance decreases with the increase of air gap, so the air gap is 37.6 mm, 100 mm, and 127 mm, respectively, and the mutual inductance of the single-turn coupling coil is analyzed with ANSYS. The mutual inductance obtained is shown in Table 1. The theoretical calculation values of the power supply system parameters of rail transit trams based on wireless charging are shown in Table 2.

On this basis, the process algorithm described in Figure 9 is used to design the coil turns. The final results are shown in Table 2. A system simulation model based on MATLAB® was built based on this set of parameters. The voltage and current waveform on the AC side of the primary and secondary side coils and the output side of the rectifier were obtained when the air gap was 100 mm, as shown in Figure 10.

The results of calculating the output power and efficiency of the system under different air gaps are shown in Table 3. The simulation results show that under the current coupling coil parameters, when the air gap fluctuation range is 37.6 mm–127 mm, the system with two systems power transmission is greater than or equal to 500 kW and the efficiency is greater than or equal to 85%.

The equivalent load of the system fluctuates due to changes in road conditions and tram loads. A MATLAB simulation model with the equivalent load of 5 Ω is built. The voltage and current waveform on the AC side of the primary and secondary side coils and the output side of the rectifier were obtained when the air gap was 100 mm, as shown in Figure 11. At this time, the output power of the system is

Table 1: Mutual inductance values at different air gaps.

Air gap/mm	37.6	100	127
Mutual inductance/μH	0.9	0.85	0.45

Table 2: Theoretical calculation values of system parameters.

Parameter	Value
Power P/kW	300
DC voltage U_{dc}/V	750
Frequency f/kHz	30
Self-inductance of primary coil L_1/μH	160.8
Self-inductance of secondary coil L_2/μH	91
Resistance of primary coil R_1/mΩ	13.1
Resistance of secondary coil R_2/mΩ	3.12
Compensates capacitor of primary coil C_1/nF	176.06
Compensates capacitor of secondary coil C_2/nF	309.55
Load R/Ω	1.51

287 kW and the efficiency is 94.1%, which can meet the overall system requirements.

To sum up, the designed coupling coil parameters can meet the requirements of power transmission greater than or equal to 500 kW and efficiency greater than or equal to 85% in the case of mutual inductance and load fluctuation.

In order to analyze the electromagnetic radiation of the coupling coil of the rail transit tram system based on wireless charging, Maxwell 3D finite element simulation software is used to simulate the different turns of the coil. The electromagnetic radiation of different turns schemes is shown in Table 4. All the parameters satisfying the system constraints are listed to obtain the optimal solution. According to the data in the table, when the number of turns of the primary coil is 2 and the number of turns of the secondary coil is 5, the electromagnetic radiation of the coupling coil of the rail transit tram based on wireless charging is the minimum.

To sum up, when the primary coil is 2 turns and the secondary coil is 5 turns, the power transmission of rail transit tram based on wireless charging technology is greater than or equal to 500 kW and the efficiency is greater than or equal to 85%. Meanwhile, the coupling coil has the minimum distance of external electromagnetic radiation. The electromagnetic radiation of rail transit tram based on wireless charging is reduced from the angle of coil design.

4.2. Experiment. The establishment of a low-power experimental platform is shown in Figure 12. The whole system consists of 48 V DC power supply, inverter circuit, coupling coil, compensation capacitor, rectifier, boost, load, and so on. According to the parameter design method in Section 2, the parameters of the coupling coil and related parameters in the experimental platform are obtained as shown in Table 5.

Phase shift method is adopted to realize constant current control at transmitting end. The output of the system in the case of air gap fluctuation is measured experimentally. Figure 13 shows the voltage and current waveform of primary coil and secondary coil when the gap between primary coil and secondary coil is 3 cm.

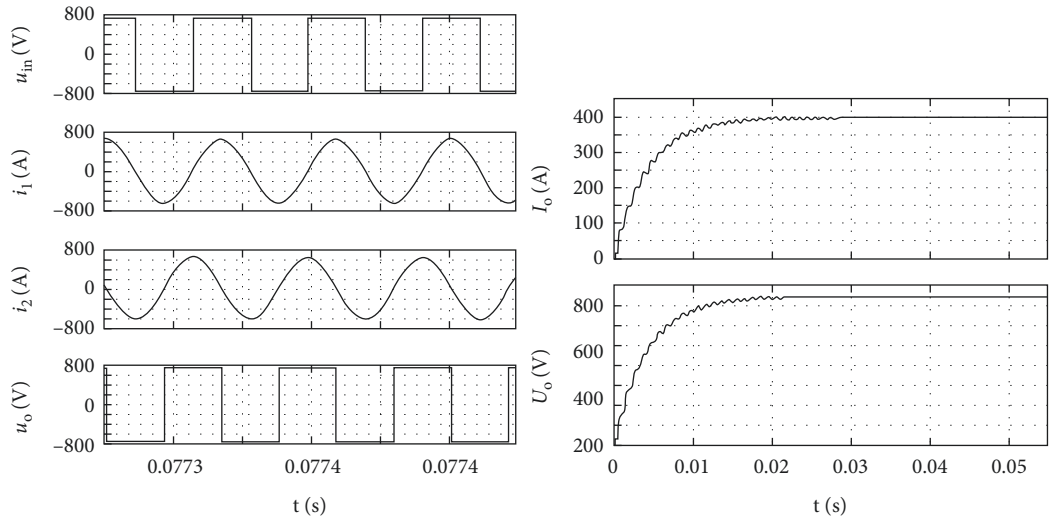

Figure 10: MATLAB simulation results when the air gap is 100 mm.

Table 3: Output power and efficiency under air gap fluctuation.

Air gap (mm)	Output power (theoretical) (kW)	Output power (simulation) (kW)	Efficiency (theoretical) (%)	Efficiency (simulation) (%)
37.6	300	299	98.95	95.6
100	298	296	98.94	95.5
127	295	292	96.53	92.3

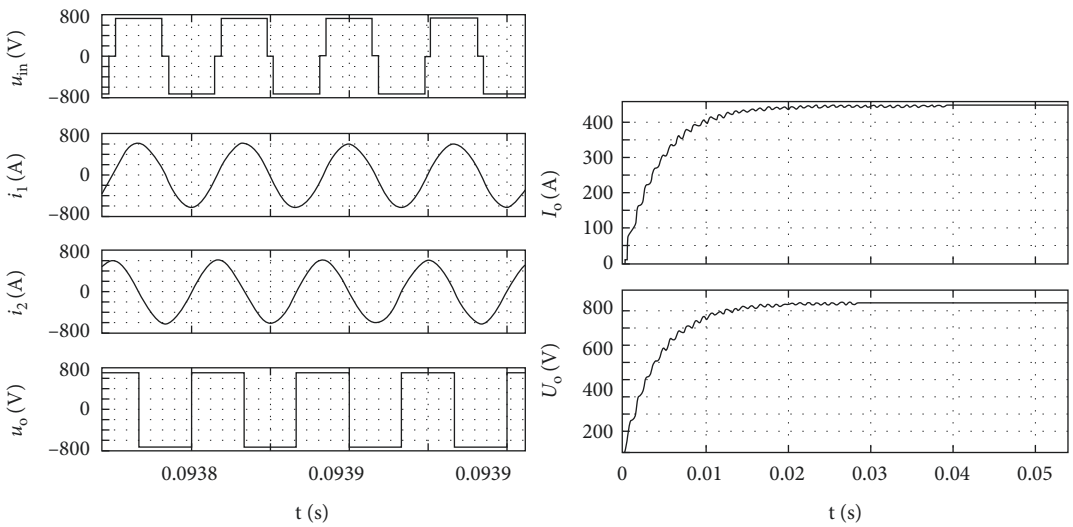

Figure 11: The equivalent load of 5 Ω MATLAB simulation results.

Table 4: Electromagnetic radiation distance.

Number of turns of primary coil N_1	Number of turns of secondary coil N_2	Electromagnetic radiation distance λ/m (theoretical)	Electromagnetic radiation distance λ/m (simulation)
2	5	3.46	3.45
3	3	3.68	3.61
4	3	3.88	3.69
5	2	4.04	3.78
6	2	4.08	3.81
10	1	4.26	4.20

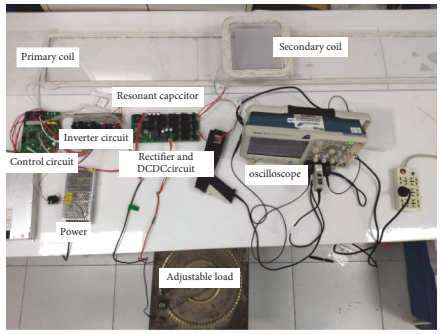

Figure 12: Experiment platform.

Table 5: System parameters.

Parameter	Value
Primary coil	2 m ∗ 0.2 m
Secondary coil	0.2 m ∗ 0.2 m
Power P/kW	1
DC voltage U_{dc}/V	48
Frequency f/kHz	30
Number of turns of primary coil N_1	8
Number of turns of secondary coil N_2	12
Self-inductance of primary coil L_1/μH	160.8
Self-inductance of secondary coil L_2/μH	91
Resistance of primary coil R_1/mΩ	13.1
Resistance of secondary coil R_2/mΩ	3.12
Compensates capacitor of primary coil C_1/nF	176.06
Compensates capacitor of secondary coil C_2/nF	309.55
Load R/Ω	1.51

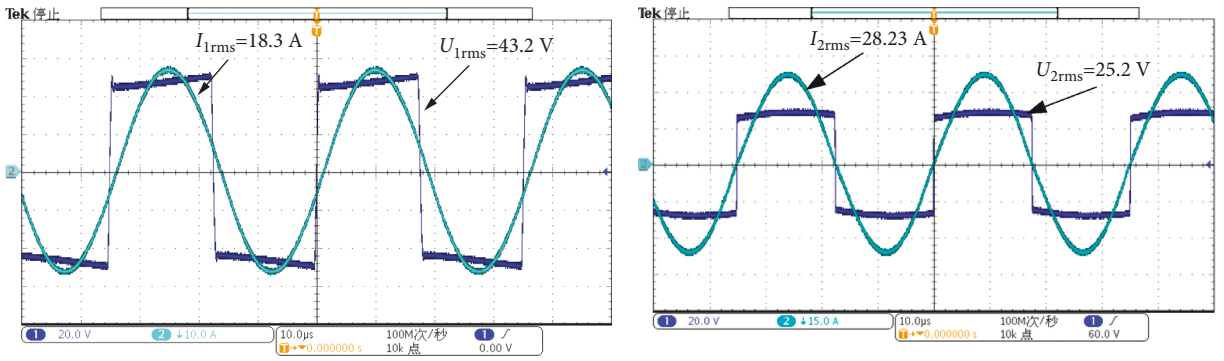

(a) (b)

Figure 13: Coupling coil voltage and current waveform of the coupling mechanism at 3 cm air gap. (a) Primary coil voltage waveform and current waveform. (b) Secondary coil voltage waveform and current waveform.

According to the calculation of the experimental results, the output power is 711.4 W, and the efficiency is 89.7%. Table 6 summarizes the output performance of the system under different air gaps and mutual inductance parameters. As shown in Table 6, in the case of air gap fluctuation of the coupling coil, the transmission efficiency of the system is more than or equal to 85%.

The output of the system is measured under load fluctuation. Figure 14 is primary coil and secondary coil voltage and current waveform when the load is 2 Ω. Table 7 summarizes the output performance of the system under different loads. As shown in Table 7, in the case of load fluctuation, the transmission efficiency of the system is more than or equal to 85%.

To sum up, under the condition of air gap and load fluctuation, the designed coil parameters can satisfy the transmission efficiency of the system which is greater than or equal to 85%.

By changing the number of coil turns, the magnetic field intensity data were measured with the magnetic field

Table 6: Output performance of the system under different air gaps.

Air gap (cm)	1	3	5
Output power (theoretical) (W)	775.4	897.8	684.5
Output power (simulation) (W)	764.4	870.5	603.4
Output power (experiment) (W)	506.9	711.4	521.0
Efficiency (theoretical) (%)	97.5	99.1	99.2
Efficiency (simulation) (%)	96.4	95.4	92.3
Efficiency (experiment) (%)	90.6	89.7	85.3

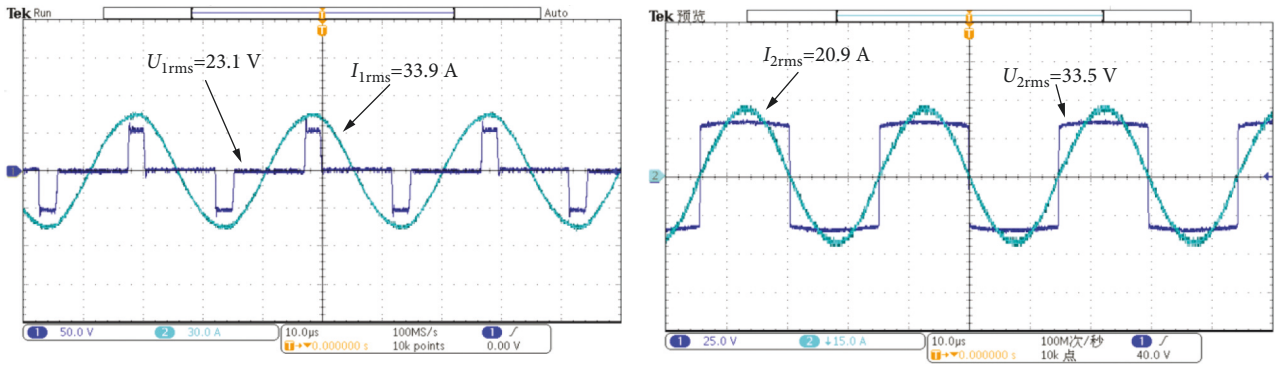

(a) (b)

Figure 14: Coupling coil voltage and current waveform of the coupling mechanism at load 2 Ω. (a) Primary coil voltage waveform and current waveform. (b) Secondary coil voltage waveform and current waveform.

Table 7: Output of the system under different load parameters.

Load/Ω	1	2	3.2
Output power (theoretical) (W)	720.1	897.8	835.2
Output power (simulation) (W)	698.3	870.5	805.8
Output power (experiment) (W)	574.7	711.4	693.3
Efficiency (theoretical) (%)	99.2	99.1	98.3
Efficiency (simulation) (%)	96.6	95.4	91.0
Efficiency (experiment) (%)	90.2	89.7	85.3

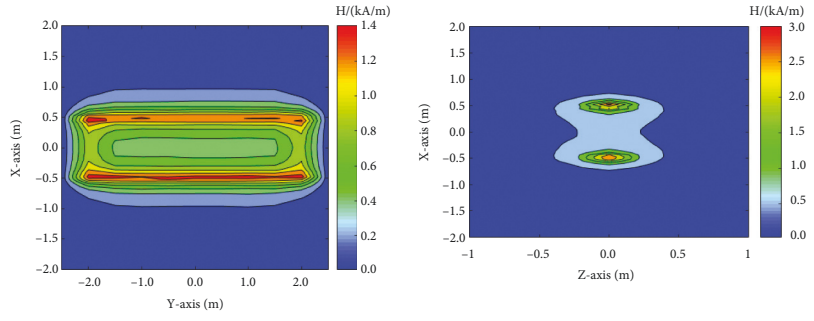

(a) (b)

Figure 15: Magnetic field strength of coupling coil. (a) The distribution of magnetic field strength in the *XY* plane. (b) The distribution of magnetic field strength in the *XZ* plane.

measuring instrument, and the relevant data were imported into MATLAB® for drawing, so as to obtain the magnetic field distribution of the coupling coil. Figure 15 shows the magnetic field distribution in the *XY* horizontal plane and the *XZ* vertical plane at the height of 100 mm when the number of turns of the primary coil is 8 and the number of turns of the secondary coil is 12. Because the experimental space is limited, the electromagnetic radiation distance is expressed by measuring the magnetic field intensity at the same location. Use model 8030 Gauss/Tesla meter for

Table 8: Electromagnetic radiation distance.

Number of turns of primary coil N_1	6	8	12
Number of turns of secondary coil N_2	16	12	8
Magnetic field strength (theoretical) H (A/m)	39.5	54.2	60.0
Magnetic field strength (simulation) H (A/m)	40.8	56.6	61.7
Magnetic field strength (experiment) H (A/m)	39.4	53.5	63.4

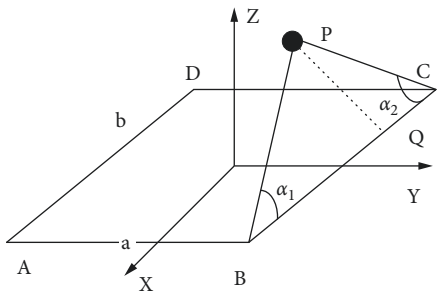

Figure 16: Rectangular coil magnetic field calculation diagram.

measurement. The electromagnetic radiation distance of different coil turns is shown in Table 8.

In conclusion, the coupling coil design scheme with 8 turns of the primary coil and 12 turns of the secondary side coil can meet the requirement that the power transmission efficiency of rail transit trams based on wireless charging is greater than or equal to 85% in the case of air gap fluctuation and load fluctuation. At the same time, the distance of external electromagnetic radiation of the coupling coil is minimum. Simulation and experimental results show the effectiveness and feasibility of the design method. By the angle of coil design, the external electromagnetic radiation of rail transit trams based on wireless charging is reduced, and the electromagnetic safety of rail transit trams based on wireless charging is guaranteed.

5. Conclusion

The dynamic charging system of a wireless charging tram puts forward strict requirements on the output power and efficiency of the system. Unreasonable parameter design will lead to excessive external electromagnetic radiation of the system, which will affect the normal operation of equipment in the surrounding environment and the safety of human body. In this paper, combining with the actual installation space of rail transit tram, a set of design algorithm for induction coupling coil parameters of wireless rechargeable tram is proposed, and the coil parameters are designed with minimum electromagnetic radiation as the goal. Simulation and experimental results show that the method proposed in this paper can effectively select the optimal coil parameters that meet the system requirements. And it can effectively reduce electromagnetic radiation when the system constraints are satisfied. The results show that the parameter design method is feasible and effective and has high engineering application value.

Nomenclature

U_{dc}, U_o: Input and output DC voltage source
U_1: Full bridge ac voltage
U_2: Diode rectifier ac voltage
R: Diode rectifier equivalent resistance
R_L: Load resistance
ω: Resonant frequency
L_1, L_2: Transformer primary and secondary self-inductances
L_{10}, L_{20}: Single turn transformer primary and secondary self-inductances
C_1, C_2: Primary and secondary series compensating capacitors
R_1, R_2: Transformer primary and secondary self-resistances
Z_1, Z_2: Transformer primary and secondary impedance
P_{out}: Output power
η: Transmission efficiency
M: Mutual inductance
M_0: Single to single mutual inductance
μ_0, μ: Permeability in vacuum and wire
a, b, r: Length, width, and the cross-section radius of the rectangular coil wire
A: Magnetic vector
$\mathbf{J}$: Electric current density
B: Magnetic induction
$\mathbf{H}$: Magnetic field intensity.

Appendix

A rectangular coil center as the origin of coordinates, parallel to the BC side for the X axis, vertical X axis to the Y axis, perpendicular to the axis of the coil in the flat for the Z axis, coil length AB is $2a$, width BC is $2b$, in the region of the wireless charging without metal materials in any point P (x, y, z) are shown in Figure 16.

The rectangular coil is regarded as four segments of direct current-carrying wire of finite length, each of which is calculated, and then the magnetic induction intensity generated by a segment of direct current-carrying wire at any measuring point in space is obtained by means of vector superposition.

$$B = \frac{\mu_0 I}{4\pi R}\left(\cos\alpha_1 - \cos\alpha_2\right), \tag{A.1}$$

where

$$R = \sqrt{(a-x)^2 + z^2},$$

$$\cos\alpha_1 = \frac{b+y}{\sqrt{(a-x)^2 + (b+y)^2 + z^2}}, \tag{A.2}$$

$$\cos\alpha_2 = \frac{b-y}{\sqrt{(a-x)^2 + (b-y)^2 + z^2}}.$$

It can be obtained that the magnetic induction intensity generated by BC edge at point P is

$$B_{BC} = \frac{\mu I}{4\pi\sqrt{(a-x)^2+z^2}}\left(\frac{b+y}{\sqrt{(a-x)^2+(b+y)^2+z^2}} + \frac{b-y}{\sqrt{(a-x)^2+(b-y)^2+z^2}}\right). \tag{A.3}$$

According to the right hand helix, BBC is perpendicular to PQ and is in a right hand helix relationship with the current. Therefore, BBC is decomposed in the X, Y, and Z directions, and the results are as follows:

$$\begin{aligned} B_{BCX} &= \frac{\mu I z}{4\pi\left[(a-x)^2+z^2\right]}\left(\frac{b+y}{\sqrt{(a-x)^2+(b+y)^2+z^2}} + \frac{b-y}{\sqrt{(a-x)^2+(b-y)^2+z^2}}\right), \\ B_{BCY} &= 0, \\ B_{BCZ} &= \frac{\mu I (a-x)}{4\pi\left[(a+x)^2+z^2\right]}\left(\frac{b-y}{\sqrt{(a+x)^2+(b-y)^2+z^2}} + \frac{b+y}{\sqrt{(a+x)^2+(b+y)^2+z^2}}\right). \end{aligned} \tag{A.4}$$

Similarly, magnetic induction intensities of AB, CD, and AD edges to point P can be obtained, respectively. By means of vector superposition, the total magnetic induction intensity generated by a single rectangular coil at point P can be obtained

$$B_x = \frac{\mu I}{4\pi}\left[\begin{array}{l} \dfrac{z}{\left[(a-x)^2+z^2\right]}\left(\dfrac{b+y}{\sqrt{(a-x)^2+(b+y)^2+z^2}} + \dfrac{b-y}{\sqrt{(a-x)^2+(b-y)^2+z^2}}\right) \\ -\dfrac{z}{\left[(a+x)^2+z^2\right]}\left(\dfrac{b-y}{\sqrt{(a+x)^2+(b-y)^2+z^2}} + \dfrac{b+y}{\sqrt{(a+x)^2+(b+y)^2+z^2}}\right) \end{array}\right],$$

$$B_y = \frac{\mu I}{4\pi}\left[\begin{array}{l} \dfrac{z}{\left[(b-y)^2+z^2\right]}\left(\dfrac{a+x}{\sqrt{(a+x)^2+(b+y)^2+z^2}} + \dfrac{a-x}{\sqrt{(a-x)^2+(b+y)^2+z^2}}\right) \\ -\dfrac{(b-y)}{\left[(a+x)^2+z^2\right]}\left(\dfrac{a+x}{\sqrt{(a+x)^2+(b+y)^2+z^2}} + \dfrac{a-x}{\sqrt{(a-x)^2+(b+y)^2+z^2}}\right) \end{array}\right],$$

$$B_z = \frac{\mu I}{4\pi}\left[\begin{array}{l} \dfrac{(b+y)}{\left[(b-y)^2+z^2\right]}\left(\dfrac{a+x}{\sqrt{(a+x)^2+(b+y)^2+z^2}}+\dfrac{a-x}{\sqrt{(a-x)^2+(b+y)^2+z^2}}\right) \\ +\dfrac{(b-y)}{\left[(b-y)^2+z^2\right]}\left(\dfrac{a+x}{\sqrt{(a+x)^2+(b-y)^2+z^2}}+\dfrac{a-x}{\sqrt{(a-x)^2+(b-y)^2+z^2}}\right) \\ +\dfrac{(a-x)}{\left[(a-x)^2+z^2\right]}\left(\dfrac{b+y}{\sqrt{(a-x)^2+(b+y)^2+z^2}}+\dfrac{b-y}{\sqrt{(a-x)^2+(b-y)^2+z^2}}\right) \\ +\dfrac{(a+x)}{\left[(a+x)^2+z^2\right]}\left(\dfrac{b-y}{\sqrt{(a+x)^2+(b-y)^2+z^2}}+\dfrac{b+y}{\sqrt{(a+x)^2+(b+y)^2+z^2}}\right) \end{array}\right]. \tag{A.5}$$

The resultant electromagnetic induction intensity of two coaxial parallel rectangular current-carrying coils at any point is obtained by means of vector superposition.

$$B_x = \frac{\mu I_1}{4\pi}\left[\begin{array}{l} \dfrac{z-c}{\left[(a_1-x)^2+(z-c)^2\right]}\left(\dfrac{b_1+y}{\sqrt{(a_1-x)^2+(b_1+y)^2+(z-c)^2}}+\dfrac{b_1-y}{\sqrt{(a_1-x)^2+(b_1-y)^2+(z-c)^2}}\right) \\ -\dfrac{z-c}{\left[(a_1+x)^2+(z-c)^2\right]}\left(\dfrac{b_1-y}{\sqrt{(a_1+x)^2+(b_1-y)^2+(z-c)^2}}+\dfrac{b_1+y}{\sqrt{(a_1+x)^2+(b_1+y)^2+(z-c)^2}}\right) \end{array}\right]$$

$$+\frac{\mu I_2}{4\pi}\left[\begin{array}{l} \dfrac{z+c}{\left[(a_2-x)^2+z^2\right]}\left(\dfrac{b_2+y}{\sqrt{(a_2-x)^2+(b_2+y)^2+(z+c)^2}}+\dfrac{b_2-y}{\sqrt{(a_2-x)^2+(b_2-y)^2+(z+c)^2}}\right) \\ -\dfrac{z+c}{\left[(a_2+x)^2+(z+c)^2\right]}\left(\dfrac{b_2-y}{\sqrt{(a_2+x)^2+(b_2-y)^2+(z+c)^2}}+\dfrac{b_2+y}{\sqrt{(a_2+x)^2+(b_2+y)^2+(z+c)^2}}\right) \end{array}\right],$$

$$B_y = \frac{\mu I_1}{4\pi}\left[\begin{array}{l} \dfrac{z-c}{\left[(b_1-y)^2+(z-c)^2\right]}\left(\dfrac{a_1+x}{\sqrt{(a_1+x)^2+(b_1+y)^2+(z-c)^2}}+\dfrac{a_1-x}{\sqrt{(a_1-x)^2+(b_1+y)^2+(z-c)^2}}\right) \\ -\dfrac{(b_1-y)}{\left[(a_1+x)^2+(z-c)^2\right]}\left(\dfrac{a_1+x}{\sqrt{(a_1+x)^2+(b_1+y)^2+(z-c)^2}}+\dfrac{a_1-x}{\sqrt{(a_1-x)^2+(b_1+y)^2+(z-c)^2}}\right) \end{array}\right]$$

$$+\frac{\mu I_2}{4\pi}\left[\begin{array}{l} \dfrac{z+c}{\left[(b_2-y)^2+(z+c)^2\right]}\left(\dfrac{a_2+x}{\sqrt{(a_2+x)^2+(b_2+y)^2+(z+c)^2}}+\dfrac{a_2-x}{\sqrt{(a_2-x)^2+(b_2+y)^2+(z+c)^2}}\right) \\ -\dfrac{(b_2-y)}{\left[(a_2+x)^2+(z+c)^2\right]}\left(\dfrac{a_2+x}{\sqrt{(a_2+x)^2+(b_2+y)^2+(z+c)^2}}+\dfrac{a_2-x}{\sqrt{(a_2-x)^2+(b_2+y)^2+(z+c)^2}}\right) \end{array}\right],$$

$$B_z = \frac{\mu I_1}{4\pi}\left[\begin{array}{l}\dfrac{(b_1+y)}{\left[(b_1-y)^2+(z-c)^2\right]}\left(\dfrac{a_1+x}{\sqrt{(a_1+x)^2+(b_1+y)^2+(z-c)^2}}+\dfrac{a_1-x}{\sqrt{(a_1-x)^2+(b_1+y)^2+(z-c)^2}}\right)\\ +\dfrac{(b_1-y)}{\left[(b_1-y)^2+(z-c)^2\right]}\left(\dfrac{a_1+x}{\sqrt{(a_1+x)^2+(b_1-y)^2+(z-c)^2}}+\dfrac{a_1-x}{\sqrt{(a_1-x)^2+(b_1-y)^2+(z-c)^2}}\right)\\ +\dfrac{(a_1-x)}{\left[(a_1-x)^2+(z-c)^2\right]}\left(\dfrac{b_1+y}{\sqrt{(a_1-x)^2+(b_1+y)^2+(z-c)^2}}+\dfrac{b_1-y}{\sqrt{(a_1-x)^2+(b_1-y)^2+(z-c)^2}}\right)\\ +\dfrac{(a_1+x)}{\left[(a_1+x)^2+(z-c)^2\right]}\left(\dfrac{b_1-y}{\sqrt{(a_1+x)^2+(b_1-y)^2+(z-c)^2}}+\dfrac{b_1+y}{\sqrt{(a_1+x)^2+(b_1+y)^2+(z-c)^2}}\right)\end{array}\right] + \frac{\mu I_2}{4\pi}\left[\begin{array}{l}\dfrac{(b_2+y)}{\left[(b_2-y)^2+(z+c)^2\right]}\left(\dfrac{a_2+x}{\sqrt{(a_2+x)^2+(b_2+y)^2+(z+c)^2}}+\dfrac{a_2-x}{\sqrt{(a_2-x)^2+(b_2+y)^2+(z+c)^2}}\right)\\ +\dfrac{(b_2-y)}{\left[(b_2-y)^2+(z+c)^2\right]}\left(\dfrac{a_2+x}{\sqrt{(a_2+x)^2+(b_2-y)^2+(z+c)^2}}+\dfrac{a_2-x}{\sqrt{(a_2-x)^2+(b_2-y)^2+(z+c)^2}}\right)\\ +\dfrac{(a_2-x)}{\left[(a_2-x)^2+(z+c)^2\right]}\left(\dfrac{b_2+y}{\sqrt{(a_2-x)^2+(b_2+y)^2+(z+c)^2}}+\dfrac{b_2-y}{\sqrt{(a_2-x)^2+(b_2-y)^2+(z+c)^2}}\right)\\ +\dfrac{(a_2+x)}{\left[(a_2+x)^2+(z+c)^2\right]}\left(\dfrac{b_2-y}{\sqrt{(a_2+x)^2+(b_2-y)^2+(z+c)^2}}+\dfrac{b_2+y}{\sqrt{(a_2+x)^2+(b_2+y)^2+(z+c)^2}}\right)\end{array}\right]. \tag{A.6}$$

For the multi-turn coil, it can be equivalent to several concentric rectangular coils, and the magnetic induction intensity can be obtained by vector superposition.

Data Availability

The Control Ideas of reference ([1–20]) data used to support the findings of this study have been deposited in the [DOI] repository. Requests for access to these data should be made to CNKI [WWW.CNKI.COM.CN].

Conflicts of Interest

The authors declare that they have no conflicts of interest.

Acknowledgments

This work was supported by the National Key Research and Development Program under Grant 2021YFB1600203.

References

[1] L. Shi, Z. Yin, L. Jiang, and Y. Li, "Advances in inductively coupled power transfer technology for rail transit," *CES Transactions on Electrical Machines and Systems*, vol. 1, no. 4, pp. 383–396, 2017.

[2] Y. Li, W. Sun, X. Zhu, and J. Hu, "A hybrid modulation control for wireless power transfer systems to improve efficiency under light-load conditions," *IEEE Transactions on Industrial Electronics*, vol. 69, no. 7, pp. 6870–6880, 2022.

[3] Y. Li, R. Mai, L. Ma, and Z. He, "Dual parallel wound primary coil based IPT systems and its power allocation technique," *Proceedings of the CSEE*, vol. 35, no. 17, pp. 4454–4460, 2015.

[4] M. Fan, L. Shi, Z. Yin, L. Jiang, and F. Zhang, "Research on control strategy of segmented power supply for mobile inductive power transfer system," *Transactions of China Electrotechnical Society*, vol. 33, no. 17, pp. 3998–4006, 2018.

[5] Y. Li, S. Liu, X. Zhu, and J. M. R. Z. Hu, "Extension of ZVS region of series-series WPT systems by an auxiliary variable inductor for improving efficiency," *IEEE Transactions on Power Electronics*, vol. 36, no. 7, pp. 7513–7525, July 2021.

[6] F. Y. Lin, G. A. Covic, and J. T. Boys, "Evaluation of magnetic pad sizes and topologies for electric vehicle charging," *IEEE Transactions on Power Electronics*, vol. 30, no. 11, pp. 6391–6407, 2015.

[7] C. Hu, Y. Sun, and X. Lv, "Magnetic coupler design procedure for IPT system and its application to EV's wireless charging," *International Journal of Applied Electromagnetics and Mechanics*, vol. 47, no. 3, pp. 861–873, 2015.

[8] L. Xu, Y. Du, and L. Shi, "Reluctancecircuit and structure optimization of contactless transformer," *Advanced Technology of Electrical Engineering and Energy*, vol. 37, no. 1, pp. 15–22, 2018.

[9] Y. Geng, Z. Yang, F. Lin, and W. Junchao, "Characteristic analysis of multiple-receiving coupling coil mode for wireless power transfer systems," *Transactions of China Electrotechnical Society*, vol. 32, no. S2, pp. 1–9, 2017.

[10] Y.-G. Su, S. Zhang, C. Hu, and C. S. W. Tang, "An embeddable transmitter coil applied to electric vehicles powered by IPT system," *International Journal of Applied Electromagnetics and Mechanics*, vol. 50, no. 4, pp. 627–636, 2016.

[11] W. Hao, L. Zhang, S. Xiu, and C. Yang, "Load segment tracking control of IPT system based on power efficiency optimization," *IEEE Access*, vol. 8, no. 1, pp. 7070–7080, 2020.

[12] Icnirp Safety Guideline, "Guidelines for limiting exposure to time-varying electric and magnetic fields (1 Hz to 100 kHz)," *Health Physics*, vol. 99, no. 6, pp. 818–836, 2010.

[13] Q. Wang, W. Li, J. Kang, and Y. Wang, "Electromagnetic safety of magnetic resonant wireless charging system in electric vehicles," in *Proceedings of the 2017 IEEE PELS Workshop on Emerging Technologies: Wireless Power Transfer (WoW)*, pp. 1–6, Chongqing, China, May 2017.

[14] P.-P. Ding, L. Bernard, L. Pichon, and A. Razek, "Evaluation of electromagnetic fields in human body exposed to wireless inductive charging system," *IEEE Transactions on Magnetics*, vol. 50, no. 2, pp. 1037–1040, 2014.

[15] H. Hua Cai, L. Liming Shi, and Y. Yaohua Li, "Harmonic-based phase-shifted control of inductively coupled power transfer," *IEEE Transactions on Power Electronics*, vol. 29, no. 2, pp. 594–602, 2014.

[16] T. Linlin, H. Xueliang, L. Hui, and H. Hui, "Study of wireless power transfer system through strongly coupled resonances," in *Proceedings of the 2010 International Conference on Electrical and Control Engineering*, pp. 4275–4278, Wuhan, China, June 2010.

[17] G. Zheng, "Optimization design of efficient middle distance magnetic-resonance wireless charge coil suitable for electric vehicle charging[J]," *Transactions of China Electrotechnical Society*, vol. 32, no. S1, pp. 209–216, 2017.

[18] H. Cai, L. Shi, and Y. Li, "Output power adjustment in inductively coupled power transfer system," *Transactions of China Electrotechnical Society*, vol. 29, no. 1, pp. 215–220, 2014.

[19] W. Hao, liwei Zhang, and S. Xiu, "Decoupling control strategy of IPT system based on optimal efficiency load tracking," *Journal of Advanced Transportation*, vol. 2019, Article ID 9182761, Apr. 2019.

[20] M. Budhia, J. T. Boys, G. A. Covic, and C.-Y. Huang, "Development of a single-sided flux magnetic coupler for electric vehicle IPT charging systems," *IEEE Transactions on Industrial Electronics*, vol. 60, no. 1, pp. 318–328, 2013.